

# Radiative engineering of plasmon lifetimes in embedded nanoantenna arrays

Ronen Adato,<sup>1,2,5</sup> Ahmet Ali Yanik,<sup>1,2,5</sup> Chih-Hui Wu,<sup>3</sup> Gennady Shvets,<sup>3</sup>  
and Hatice Altug<sup>1,2,4\*</sup>

<sup>1</sup>Department of Electrical and Computer Engineering, Boston University, Boston, MA, 02215, USA

<sup>2</sup>Boston University Photonics Center, Boston, MA, 02215, USA

<sup>3</sup>Department of Physics, The University of Texas at Austin, Austin, TX, 78712, USA

<sup>4</sup>Material Science Division, Boston, MA, 02215, USA

<sup>5</sup>These authors contributed equally.

\*altug@bu.edu

**Abstract:** It is generally accepted that the lifetimes of the localized plasmonic excitations are inherently controlled by the type of the metals and the shape of the nanoparticles. However, extended plasmonic lifetimes and enhanced near-fields in nanoparticle arrays can be achieved as a result of collective excitation of plasmons. In this article, we demonstrate significantly longer plasmon lifetimes and stronger near-field enhancements by embedding the nanoantenna arrays into the substrate. Our approach offers a more homogeneous dielectric background allowing stronger diffractive couplings among plasmonic particles leading to strong suppression of the radiative damping. We observe near-field enhancements well beyond than those achievable with isolated nanoparticles. Enhanced fields obtained in these structures could be attractive for biosensing and non-linear photonics applications.

© 2010 Optical Society of America

**OCIS codes:** (240.6680) Optics at surfaces: Surface plasmons; (260.3910) Physical optics: Metal optics; (250.5403) Optoelectronics: Plasmonics.

---

## References and links

1. E. Ozbay, "Plasmonics: merging photonics and electronics at nanoscale dimensions," *Science* **311**(5758), 189–193 (2006).
2. S. Lal, S. Link, and N. J. Halas, "Nano-optics from sensing to waveguiding," *Nat. Photonics* **1**(11), 641–648 (2007).
3. M. I. Stockman, V. M. Shalaev, M. Moskovits, R. Botet, and T. F. George, "Enhanced Raman scattering by fractal clusters: Scale invariant theory," *Phys. Rev. B* **46**(5), 2821–2830 (1992).
4. K. Kneipp, Y. Wang, H. Kneipp, L. T. Perelman, I. Itzkan, R. R. Dasari, and M. S. Feld, "Single molecule detection using surface-enhanced Raman scattering (SERS)," *Phys. Rev. Lett.* **78**(9), 1667–1670 (1997).
5. R. Adato, A. A. Yanik, J. J. Amsden, D. L. Kaplan, F. G. Omenetto, M. K. Hong, S. Erramilli, and H. Altug, "Ultra-sensitive vibrational spectroscopy of protein monolayers with plasmonic nanoantenna arrays," *Proc. Natl. Acad. Sci. U.S.A.* **106**(46), 19227–19232 (2009).
6. F. Neubrech, A. Pucci, T. W. Cornelius, S. Karim, A. García-Etxarri, and J. Aizpurua, "Resonant plasmonic and vibrational coupling in a tailored nanoantenna for infrared detection," *Phys. Rev. Lett.* **101**(15), 157403 (2008).
7. E. J. Sánchez, L. Novotny, and X. S. Xie, "Near-field fluorescence microscopy based on two-photon excitation with metal tips," *Phys. Rev. Lett.* **82**(20), 4014–4017 (1999).
8. V. E. Ferry, L. A. Sweatlock, D. Pacifici, and H. A. Atwater, "Plasmonic nanostructure design for efficient light coupling into solar cells," *Nano Lett.* **8**(12), 4391–4397 (2008).
9. A. Artar, A. A. Yanik, and H. Altug, "Fabry-Perot nanocavities in multilayered plasmonic crystals for enhanced biosensing," *Appl. Phys. Lett.* **95**(5), 051105 (2009).
10. A. A. Yanik, R. Adato, S. Erramilli, and H. Altug, "Hybridized nanocavities as single-polarized plasmonic antennas," *Opt. Express* **17**(23), 20900–20910 (2009).
11. J. Homola, S. S. Yee, and G. Gauglitz, "Surface plasmon resonance sensors: review," *Sens. Actuators B Chem.* **54**(1-2), 3–15 (1999).
12. I. M. White, and X. Fan, "On the performance quantification of resonant refractive index sensors," *Opt. Express* **16**(2), 1020–1028 (2008).
13. K.-S. Lee, and M. A. El-Sayed, "Gold and silver nanoparticles in sensing and imaging: sensitivity of plasmon response to size, shape, and metal composition," *J. Phys. Chem. B* **110**(39), 19220–19225 (2006).

14. F. Wang, and Y. R. Shen, "General properties of local plasmons in metal nanostructures," *Phys. Rev. Lett.* **97**(20), 206806 (2006).
15. C. Sönnichsen, T. Franzl, T. Wilk, G. von Plessen, J. Feldmann, O. Wilson, and P. Mulvaney, "Drastic reduction of plasmon damping in gold nanorods," *Phys. Rev. Lett.* **88**(7), 077402 (2002).
16. S. Zou, and G. C. Schatz, "Theoretical studies of plasmon resonances in one dimensional nanoparticles chains: narrow lineshapes with tunable widths," *Nanotech.* **17**(11), 2813–2820 (2006).
17. G. Della Valle, T. Söndergaard, and S. I. Bozhevolnyi, "Efficient suppression of radiation damping in resonant retardation-based plasmonic structures," *Phys. Rev. B* **79**(11), 113410 (2009).
18. V. A. Markel, "Divergence of dipole sums and the nature of non-Lorentzian exponentially narrow resonances in one-dimensional periodic arrays of nanospheres," *J. Phys. At. Mol. Opt. Phys.* **38**(7), L115–L121 (2005).
19. B. Lamprecht, G. Schider, R. T. Lechner, H. Ditlbacher, J. R. Krenn, A. Leitner, and F. R. Aussenegg, "Metal nanoparticle gratings: influence of dipolar particle interaction on the plasmon resonance," *Phys. Rev. Lett.* **84**(20), 4721–4724 (2000).
20. B. Auguié, and W. L. Barnes, "Collective resonances in gold nanoparticle arrays," *Phys. Rev. Lett.* **101**(14), 143902 (2008).
21. V. G. Kravets, F. Schedin, and A. N. Grigorenko, "Extremely narrow plasmon resonances based on diffraction coupling of localized plasmons in arrays of metallic nanoparticles," *Phys. Rev. Lett.* **101**(8), 087403 (2008).
22. Y. A. Urzhumov, and G. Shvets, "Applications of nanoparticle arrays to coherent anti-Stokes Raman spectroscopy of chiral molecules," *Proc. SPIE* **5927**, 59271D (2005).
23. C. S. T. Microwave Studio, Computer Simulation Technology, Darmstadt, Germany, <http://www.cst.com>.
24. The electric field due to point dipole are given by  

$$\mathbf{A}_j \cdot \mathbf{p}_j = k^2 \exp(ikr_j) \left\{ (\mathbf{r}_j \times \mathbf{p}_j) \times \mathbf{r}_j / r_j^3 + (1 - ikr_j) [3\mathbf{r}_j (\mathbf{r}_j \cdot \mathbf{p}_j) - r_j^2 \mathbf{p}_j] / r_j^5 \right\}$$
. The first term in the brackets has  $1/r$  dependence and corresponds to the far-field radiation. The second terms are relevant for short range interactions. In order to emphasize the importance of the phase term in the collective scattering process the interaction term is written as  $\exp(ikr_{ij}) \mathbf{C}_{ij} \cdot \mathbf{p}_j = \mathbf{A}_{ij} \cdot \mathbf{p}_j$  in the text.
25. A. D. Rakic, A. B. Djurusic, J. M. Elazar, and M. L. Majewski, "Optical properties of metallic films for vertical-cavity optoelectronic devices," *Appl. Opt.* **37**(22), 5271–5283 (1998).
26. E. D. Palik, ed., *Handbook of Optical Constants of Solids II* (Academic, Orlando, Fla., 1985).
27. M. Meier, and A. Wokaun, "Enhanced fields on large metal particles: dynamic depolarization," *Opt. Lett.* **8**(11), 581–583 (1983).
28. T. Jensen, L. Kelly, A. Lazarides and G. C. Schatz, "Electrodynamics of noble metal nanoparticles and nanoparticle clusters," *J. Clust. Sci.* **10** (1999).
29. L. Rayleigh, "On the dynamical theory of gratings," *Proc. R. Soc. Lond., A Contain. Pap. Math. Phys. Character* **79**(532), 399–416 (1907).
30. X. M. Bendaña, and F. J. Garcia de Abajo, "Confined collective excitations of self-standing and supported planar periodic particle arrays," *Opt. Express* **17**(21), 18826–18835 (2009).
31. K. B. Crozier, A. Sundaramurthy, G. S. Kino, and C. F. Quate, "Optical antennas: resonators for local field enhancement," *J. Appl. Phys.* **94**(7), 4632–4642 (2003).
32. E. Cubukcu, and F. Capasso, "Optical nanorod antennas as dispersive one-dimensional Fabry-Perot resonators for surface plasmons," *Appl. Phys. Lett.* **95**(20), 201101 (2009).
33. L. Novotny, "Effective wavelength scaling for optical antennas," *Phys. Rev. Lett.* **98**(26), 266802 (2007).
34. A. A. Yanik, X. Wang, S. Erramilli, M. K. Hong, and H. Altug, "Extraordinary midinfrared transmission of rectangular coaxial nanoaperture arrays," *Appl. Phys. Lett.* **93**(8), 081104 (2008).
35. R. Adato, *et al.*, "Ultra-sensitive vibrational spectroscopy of protein monolayers with plasmonic nanoantenna arrays – Supporting information," <http://www.pnas.org/content/106/46/19227/suppl/DCSupplemental>
36. B. Auguié, and W. L. Barnes, "Diffractive coupling in gold nanoparticle arrays and the effect of disorder," *Opt. Lett.* **34**(4), 401–403 (2009).
37. T. Klar, M. Perner, S. Grosse, G. von Plessen, W. Spirkl, and J. Feldmann, "Surface-plasmon resonances in single metallic nanoparticles," *Phys. Rev. Lett.* **80**(19), 4249–4252 (1998).

## 1. Introduction

Localized surface plasmon resonances (LSPRs) in metal nanoparticles give rise to greatly enhanced near-fields and strong far-field extinction resonances. Enhanced near-fields are attractive for applications [1,2] including Raman [3,4] and infrared absorption spectroscopies [5,6], as well as for nonlinear optical phenomena [7] and photovoltaics [8]. For other applications, narrower resonance line-widths, in addition to enhanced near-fields, could be desirable. For example, in biosensing applications based on refractive index change, the detection limit depends on both the LSPR sensitivity to the local dielectric environment and the resonance line-width [9–11]. Narrower line-widths allow smaller shifts to be detected [12]. So far, most of the effort has been concentrated on optimizing the nanoparticle geometries to improve the near-field enhancements and to control the resonance frequencies/line-widths [13–15]. Further improvements in plasmon lifetimes and near-field

enhancements require innovative approaches. Collective excitations of nanoparticle ensembles in well engineered periodic arrays offer a means to suppress radiation damping allowing improvements well beyond what is achievable by simply tuning the particle geometry [5,16–22]. In an earlier article, we demonstrated narrow far-field extinction resonances and enhanced near-fields in rod-shaped nanoparticle (nanorod) arrays as a result of suppression of the radiation damping by electromagnetic field confinement in the ensemble plane [5].

In this article, we propose and demonstrate further improvements in the near-field enhancements/line-widths by embedding the plasmonic nanoparticle arrays beneath the surface of the substrate. Far-field extinction measurements confirm the strong diffractive coupling between the particles and the resulting narrow plasmonic lineshapes. Numerical modeling using the three dimensional Finite Difference Time Domain (3D-FDTD) method [23] indicates that strong near-field enhancements complement these sharp extinction features.

## 2. Fundamentals of collective plasmonics

In an ensemble, collective plasmonic excitations arise from the retarded dipolar interactions among nanoparticles. Plasmonic behavior of the nanoparticles in an ensemble may strongly differ from that of the individual constituent nanoparticles [16,18]. This phenomenon can be understood from fundamental principles by using a coupled dipole (CD) method. For an individual nanoparticle, the acting field is simply the incident field exciting the LSPRs ( $\mathbf{E}_{act} = \mathbf{E}_{inc}$ ). A nanoparticle responds to this electric field with an induced dipole moment,  $\mathbf{p} = \alpha_p \mathbf{E}_{act}$ . In an ensemble, on the other hand, the acting field on the individual particle includes both (i) the incident field and (ii) the sum of the retarded dipolar fields due to the other nanoparticles [16,18–21]:

$$\mathbf{E}_{act,i} = \mathbf{E}_{inc,i} + \sum_{\substack{j \neq i \\ j=1}}^N e^{ikr_{ij}} \mathbf{C}_{ij} \mathbf{p}_j \quad (1)$$

where,  $\mathbf{C}_{ij}$  is the dipolar interaction matrix without the phase term [24]. The indices  $i$  and  $j$  label the  $i_{th}$  and  $j_{th}$  particles,  $r_{ij}$  is the distance between them, and  $N$  is the total number of particles. The sum in Eq. (1) strongly depends on the phase delay experienced by the retarded dipolar interactions among particles. For a periodically arranged nanoparticle array, the scattered fields add in phase at a specific wavelength when  $kr_{ij} = 2\pi m$ , where  $m$  is an integer. This corresponds to the appearance of a new grating order. For wavelengths shorter/longer than this transition wavelength, the grating order is radiative/evanescent. Interesting physical phenomena leading to the narrowing of the plasmonic resonances and the enhanced near-fields are observed around the transition wavelength. A quantitative understanding of the phenomena can be developed for an infinite chain of identical nanoparticles excited by normally incident light. In this case, dipolar moments of the constituent particles are the same  $\mathbf{p}_j = \mathbf{p}_i = \alpha_p \mathbf{E}_{act,i}$  and Eq. (1) can be simplified to:

$$\mathbf{E}_{act,i} = \mathbf{E}_{inc,i} + \underbrace{\left( \sum_{\substack{j \neq i \\ j=1}}^N e^{ikr_{ij}} \mathbf{C}_{ij} \right)}_S \alpha_p \mathbf{E}_{act,i} \quad (2)$$

Following this relation, local electric field can be expressed as  $\mathbf{E}_{act,i} = (1 - \alpha_p S)^{-1} \mathbf{E}_{inc,i}$ , where  $S$  is the retarded dipole sum defined in the parentheses in Eq. (2). Accordingly, an effective polarizability for nanoparticles can be defined as:

$$\alpha_{eff} = \frac{1}{1/\alpha_p - S}. \quad (3)$$

such that  $\mathbf{p}_i = \alpha_p \mathbf{E}_{act,i} = \alpha_{eff} \mathbf{E}_{inc,i}$ . This equation shows that the polarizabilities of the nanoparticles in an ensemble are controlled by the retarded dipole sum  $S$ , which is only a function of geometrical parameters. A maximum both in the imaginary part and modulus of the particle's complex polarizability, thus a peak in extinction spectrum corresponding to the array resonance, is expected when the real part of the denominator ( $1/\alpha_p - S$ ) vanishes. Creation of collective resonances can be explained using Eq. (3) for an infinite chain of nanorod particles with dimensions chosen to reflect the conditions of our experiments to be discussed below.

In Fig. 1(a) the nanoparticle polarizability,  $\alpha_p$ , and the retarded dipole sum,  $S$ , are shown with respect to the wavelength of the incident light, which is normally incident and polarized perpendicular to the chain axis (along the long axis of the nanorods). The particles are modeled as gold ellipsoids, with the dielectric function computed from a Lorentz-Drude model [25,26]. In order to account for the finite size of the particle,  $\alpha_p$  is computed using the modified long wavelength approximation (MLWA) [27,28]. Computation of  $S$  involves evaluating an infinite summation. This was done numerically with the sum terminated at  $N = 400$  particles.

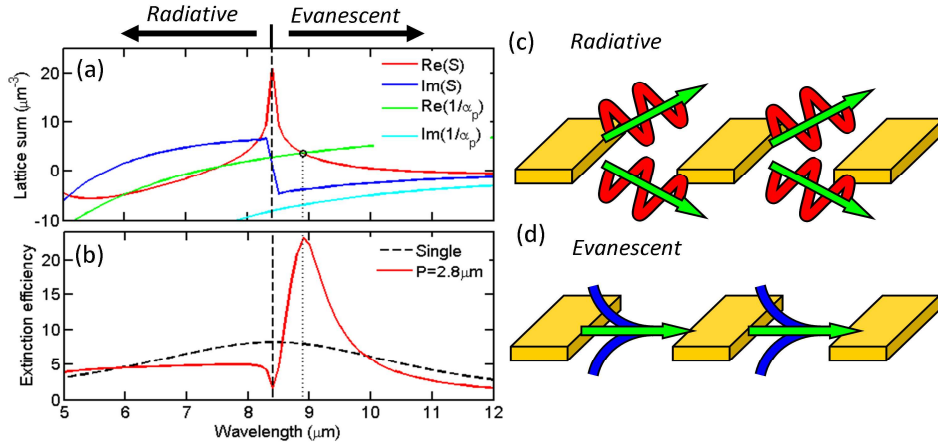


Fig. 1. Narrow extinction resonances in periodic arrays of nanoparticles. (a) Lattice sum and (b) extinction spectra are shown for 1D nanoparticle chains. The particles are gold ellipsoids with dimensions  $1.6 \times 0.3 \times 0.1 \mu\text{m}$  and the background refractive index is 3. A modified long wavelength approximation (MLWA) is used for the single particle polarizability [27,28]. The particles are arranged on a  $2.8 \mu\text{m}$  periodic chain. Light is normally incident and polarized perpendicular to the chain axis. The real part of  $S$  diverges at the grating transition wavelength (black vertical dashed line in (a)) while the imaginary part exhibits a drastic sign change. At wavelengths below (above) the transition wavelength, a grating order has radiative (c) (evanescent (d)) character.

As shown in the figure, the real part of the inverse nanoparticle polarizability (green curve) monotonously increases starting from a negative value and crosses to the positive domain at the LSPR wavelength of a single nanoparticle. The lattice sum,  $S$ , shows a more complex behavior. For large particle separations,  $C_{ij}$  is dominated by the far-field term which is a real positive number. Hence, for a periodic chain, the real part of the lattice sum  $S$  (red curve) diverges at the diffraction condition ( $kr_{ij} = 2\pi m$ ) [16,18–20]. This is visible as a sharp maximum in the figure at the grating transition wavelength (dashed vertical line).  $\text{Im}(S)$  [blue curve in Fig. 1(a)] exhibits a rapid sign change around this grating transition wavelength. Imaginary part of the lattice sum,  $\text{Im}(S)$ , is positive (negative) when the grating order is

radiative (evanescent) resulting in increased (decreased) radiative damping. The sudden appearance of the new grating order causes a dramatic increase in the radiated power from the array, which is closely associated with the Wood anomalies and Rayleigh's explanation [29]. As shown in Fig. 1(a), cancellation of the real terms in the dominator in Eq. (3) occurs at a wavelength (dotted vertical line) slightly longer than the grating transition wavelength, where the real part of  $1/\alpha_p$  (green curve) crosses the real part of lattice sum (red curve) as indicated by circle in Fig. 1(a). A maximum both in the imaginary and the modulus of the particle's complex polarizability (corresponding to resonance in extinction spectrum) is observed at this crossing wavelength, which is slightly red-shifted from the LSP resonance of the individual nanoparticle. More interestingly, the imaginary part of  $S$  is negative at the array resonance wavelength [Fig. 1(a)] and partially cancels the imaginary parts of  $1/\alpha_p$  (light blue curve in the figure). This partial cancellation results in linewidth narrowing of the far-field extinction resonance and longer plasmon lifetimes due to the suppression of the radiative damping. With increasing plasmon lifetimes, enhanced intensities in the near-field are expected as a result of field confinement in the array plane. In well engineered arrays, significant improvements in plasmon lifetimes [19] and near-field enhancements are possible [5].

For extended plasmon lifetimes and enhanced near-fields, an important consideration is that dipolar couplings among nanoparticles should be through a homogeneous dielectric background [20,30]. In practice, however, nanoparticle arrays are fabricated on substrates. For light propagating above and below the substrate, this refraction index mismatch results in different phase velocities and conditions for constructive interference. Even then, significantly narrower far-field extinction resonances, enhanced near-fields [5] and extended lifetimes [19] are observed in arrays where the nanoparticles are fabricated on a substrate [Fig. 2(b)]. However, further improvements in collective plasmonic characteristics can be achieved for arrays buried in a homogeneous background. The embedded particle geometry proposed in this article (Fig. 2) provides a largely homogeneous dielectric environment to overcome the large index mismatch limitation in conventional particle arrays.

Although index matching oils can be used to obtain a homogeneous background in experiments aimed at investigating the basic physics of the collective resonance effect [20], the embedded geometry proposed here offers several practical advantages. Firstly, greater freedom in the choice of substrate is possible, as the range of refractive indices of index matching oils is limited. This is an important consideration at the mid-infrared frequencies examined here where the substrate is silicon, with a refractive index of 3.46. Regarding biomolecule detection applications, care must be taken that the fluid used is hospitable to biological substances. This is not a concern in the embedded geometry. Finally, where enhancement in the substrate is desired, e.g. for photovoltaic and nonlinear photonic applications, the embedded geometry offers a clear advantage as will be shown with FDTD simulations.

### 3. Results

#### 3.1 Sample fabrication and measurement

We introduced a fabrication scheme for the embedded nanoparticle arrays in homogenous dielectric background as summarized in Fig. 2(a). It is based on single layer e-beam lithography, reactive ion etching (RIE) and a following lift-off process. We start by performing e-beam lithography on silicon substrates using a positive e-beam resist poly(methylmethacrylate) (PMMA). The nanohole pattern is transferred to the silicon substrate by a dry etching process using PMMA as a mask. The scanning electron microscope (SEM) image of a cleaved sample in the inset of Fig. 2(c) shows that etching is directional with vertical side-wall profile. The etch depths examined here is 200 nm. Before the removal of the PMMA mask, a directional e-beam metal deposition is performed with a thin Ti (5nm) adhesion and Au (95nm) metal layers. Lifting off the remaining resist results in well formed nanorods effectively buried beneath the substrate surface as shown in Fig. 2(d, iii-iv). On

substrate particle arrays are also fabricated [Fig. 2(d, i-ii)] to compare the effect of the homogenous versus inhomogeneous background on the collective resonances.

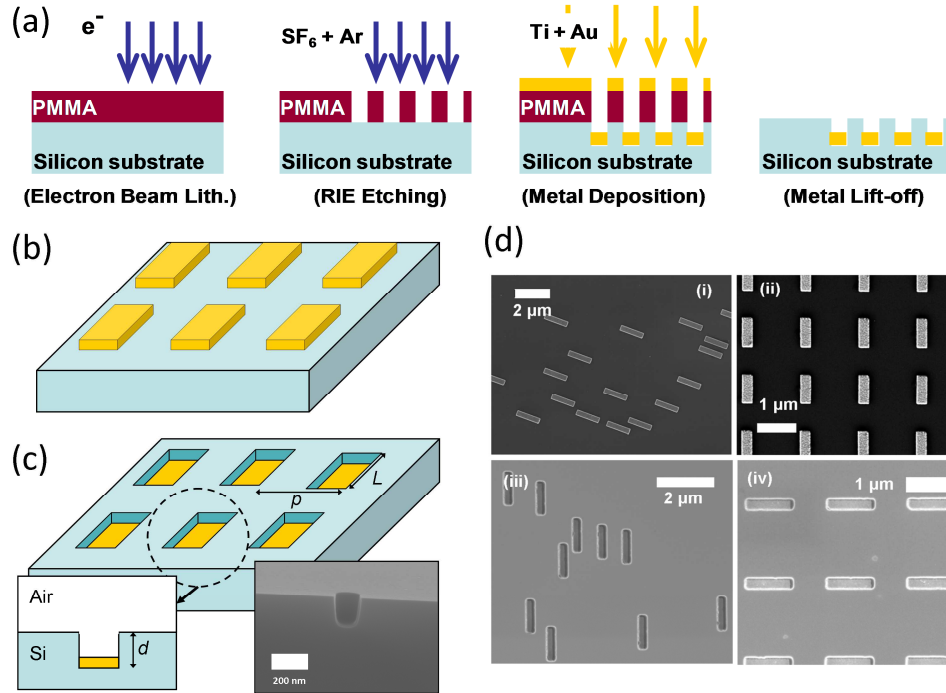


Fig. 2. Sample geometry and fabrication. The fabrication process is illustrated in (a). (b) On-substrate and (c) embedded particle array schematics are shown. Cross section view (inset) shows vertical wall profile. (d) SEM images of fabricated random array and periodic (in square lattice) samples are shown for (i, ii) –on-substrate nano-rod arrays and (iii, iv) –embedded nano-rod arrays.

In order to characterize the resonant behavior of the nanoparticle arrays, we perform transmission measurements using an IR microscope and Fourier Transform Infrared (FTIR) spectrometer. Spectra are collected over the wavelength region of 1.67–15.38  $\mu\text{m}$  ( $6000\text{--}650\text{ cm}^{-1}$ ) using a Mercury Cadmium Telluride (MCT) detector. Polarized light is incident on the particle array from the substrate side and collected with 0.4 NA, 15x reflection optics objectives. The fabrication method and the experimental conclusions that we present here, (implemented in mid-infrared spectral regime) can be readily extended to visible and near-infrared frequencies by using an appropriate etching processes on a desired substrate. Our fabrication procedure results in air holes above the embedded particles. As we show in section 3.4 using FDTD analysis, the effect of the air holes is not significant. In fact, near-field distribution of the embedded rods is found to be similar to that of a particle in a fully homogeneous background.

### 3.2 Individual particle resonances

To obtain plasmon resonances in the mid-infrared spectral region, we fabricated rod shaped particles, which support resonances similar to those of an ideal dipole antenna at wavelengths given by [31–33]

$$\lambda_{\text{Res}} = (2n_{\text{eff}} / m)L + C. \quad (4)$$

Here,  $L$  is the rod length,  $n_{\text{eff}}$  is the refractive index of the dielectric background and  $m$  is an integer corresponding to the order of the plasmonic standing wave pattern on the surface of the rod.  $C$  is a fitting parameter due to the finite width of the nanorods, which is  $C \approx 4Rn_{\text{eff}}/m$

for a cylindrical rod with cross sectional radius  $R$  and hemispherical ends [32,33]. In order to determine the individual particle response, we fabricated large arrays of randomly (but consistently oriented) particles. The random arrangement cancels out any consistent coupling among nanoparticles and allows the individual particle response to be measured at high signal to noise ratios in an interferometer [5,34]. In order to obtain consistent particle geometry throughout the random arrays, the pattern was designed to ensure that all particles were separated by at least 200 nm edge to edge. This prevented particle overlap and allowed a clean lift-off process. Experiments have shown that the array design does not affect the position of the resonance peaks [35] confirming a faithful measurement of the individual particle behavior. Spectral response of the resonance transforms to a Gaussian lineshape as the effects of particle coupling in a periodic pattern are replaced with randomly phased dipolar interactions [35,36].

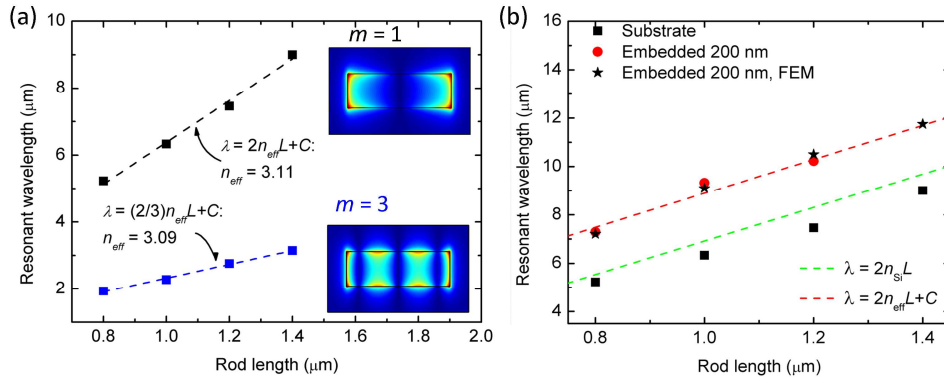


Fig. 3. (a) Length dependence of the resonance wavelength for Au rods on a Si substrate. Experimentally obtained resonances for the  $m = 1$  and  $m = 3$  modes are shown fitted to dipole antenna relation given in Eq. (4) (black and blue dashed lines, respectively). Effective indices determined from linear fits are indicated. The constant term,  $C$ , was  $0.16 \mu\text{m}$  and  $0.26 \mu\text{m}$  for the 1st and 3rd order modes, respectively. The insets correspond to the field distribution for  $z$  component of the electric field in a plane below the surface of the rod. (b) Red-shifting of the resonances is experimentally observed for embedded ( $d = 200 \text{ nm}$ ) individual antennas relative to on-substrate ( $d = 0$ ) ones. Analytical and numerical calculations based on the ideal dipole approximation (green dashed line) and 3D FEM simulations (black stars, red dashed line indicates linear fit) are shown for the embedded rods.

The lithographically patterned rods are highly rectangular, with constant heights of 100 nm, and widths of 300 nm. The rod length,  $L$ , was the only parameter of the particle geometry varied in the experiments. The linear dependence of the resonant wavelength on the rod length is clearly evident in our experimental data for  $m = 1$  and  $m = 3$  modes, as shown in Fig. 3(a). Here, the mode corresponding to  $m = 2$  is missing due to the absence of a dipole moment required to couple the incident light to this excitation. For the  $m = 1$  mode, a close fit to the dipolar antenna behavior using Eq. (4) is observed for an effective refractive index of  $n_{\text{eff}} = 3.11$  (dashed black curve). Similarly, for the  $m = 3$  mode, fitting of the experimentally observed resonance wavelengths to the dipolar antenna formula resulted in  $n_{\text{eff}} = 3.09$  (dashed blue curve).

In Fig. 3 (b), the effect of the embedding procedure on the single particle for  $m = 1$  order resonance is illustrated. Resonance wavelengths are shown for varying rod lengths and compared for on-substrate and 200 nm deep embedded rods. The resonant wavelengths for the embedded rods are strongly red-shifted in comparison with those deposited directly on the Si substrate. In addition, they deviate from those expected for an ideal half-wave dipole antenna in a Si dielectric background [Eq. (4) with  $C = 0$  indicated by green dashed line]. To confirm this observation, we have performed Finite Element Method (FEM) simulations (black stars). Experimentally observed peak positions are in very good agreement with our FEM calculations. A linear fit to the FEM data using Eq. (4) results in values of 3.51 and 1.86

$\mu\text{m}$  for  $n_{\text{eff}}$  and  $C$ , respectively. The constant term in the fit,  $C$  implies a rod with 265 nm diameter cross section, which is in close agreement with the actual width, 300 nm, of the rectangular rods. This indicates that finite width of the particle is not negligible for embedded nanorods and results in red-shifting.

### 3.3 Collective resonances in embedded periodic arrays

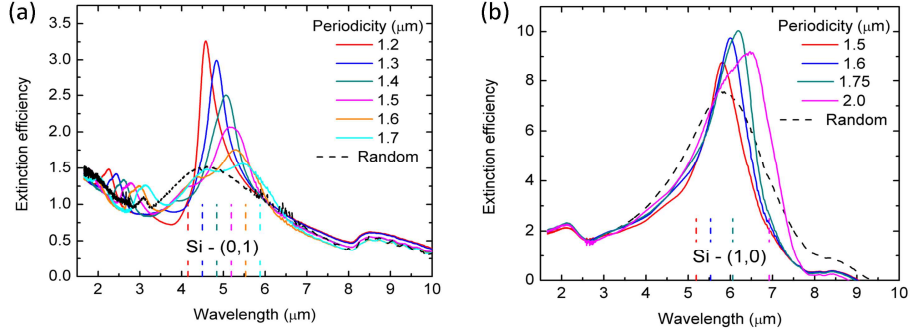


Fig. 4. Extinction spectra for (a) embedded ( $d = 200$  nm) and (b) on-substrate arrays are shown with changing periodicity. The diffraction edges are indicated by the dashed vertical lines at the bottom of the figures. The feature at  $\sim 8\mu\text{m}$  in (a) is associated with the formation of a thin oxide layer on the Si substrates. (b) is adapted from PNAS [5]. The individual particle spectra obtained from random arrays are shown for comparison purposes (dashed black lines).

Significantly narrower resonances as well as enhanced extinction efficiencies are demonstrated for well optimized periodic arrays (in square lattice), buried  $d = 200$  nm beneath the silicon surface (Fig. 4). The resonance wavelengths/linewidths as well as the extinction efficiencies strongly depend on the array periodicity, a sign for stronger diffractive and plasmonic coupling compared to the on-substrate arrays. The results here are presented for embedded nanorod particles with  $L = 500$  nm and on substrate rods with  $L = 1100$  nm such that the individual particle resonance wavelengths are comparable. In well optimized arrays, a quality factor improvement of  $Q_{\text{array}}/Q_{\text{ind}} = 4.6$  over that of an individual nanoparticle is observed due to the suppression of the radiative losses [Fig. 4(a)]. As shown in Fig. 4(b) (adapted from [5]), narrowing of plasmon resonances of on-substrate arrays is weaker than that of the periodic arrays embedded in silicon substrate. Improvements in quality factors for on-substrate arrays are limited to  $Q_{\text{array}}/Q_{\text{ind}} = 2$  due to weaker collective excitation of plasmons. Although this figure may seem to be modest, the fact that near field enhancements are correlated with but not linearly proportional with quality factor improvements must be also taken into consideration [17,37]. In fact, in an earlier article, we have obtained an order of magnitude improved absorption signals for a quality factor improvement of only  $Q_{\text{array}}/Q_{\text{ind}} = 2$  leading to signal enhancements of  $10^4$ - $10^5$  with zepto mole level sensitivities [5]. Thus, higher quality factor improvements obtained in this article ( $Q_{\text{array}}/Q_{\text{ind}} = 4.6$ ) could lead to even greater near-field enhancements as we show in the FDTD analysis below. As shown in Fig. 4(a), additional resonances at shorter wavelengths are observed for the embedded arrays. These resonances are associated to the diffractive (Wood's) anomalies. They are controlled by the array periodicity and show no variation in their line-widths. The plasmonic excitation modes (both  $m = 1$  and  $m = 3$ ) are spectrally far from these shorter wavelength resonances thus plasmons have no effect on these anomalies. Such short wavelength anomalies are absent in the extinction measurements obtained from on-substrate arrays as a result of diminished diffractive couplings [Fig. 4(b)].

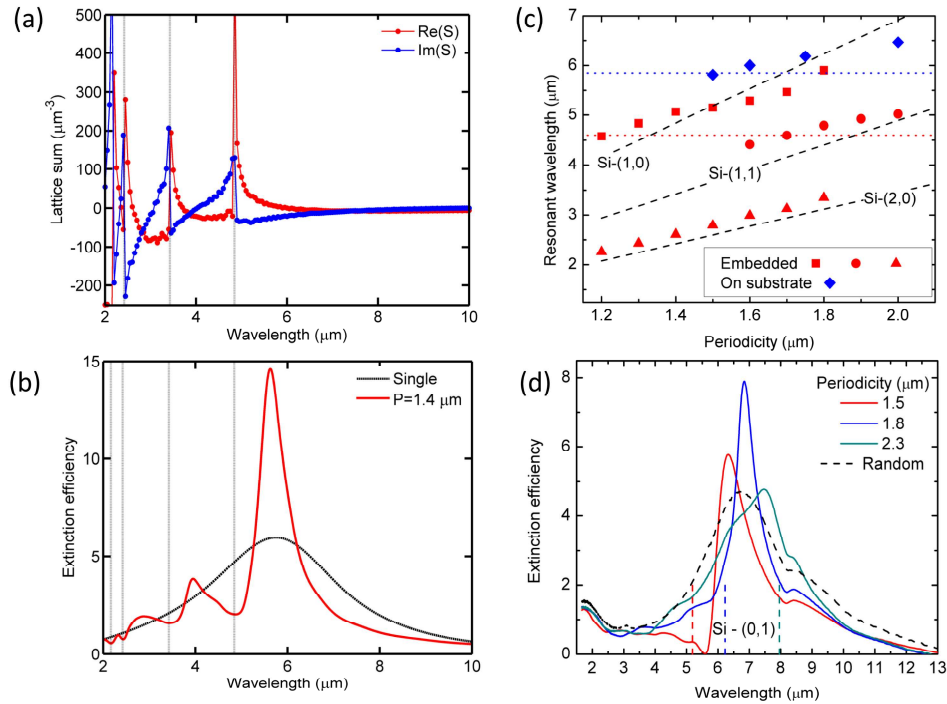


Fig. 5. The strong effect of array periodicity on extinction spectra is illustrated. (a) Real and imaginary parts of the lattice sum ( $S$ ) for a 2D periodic ( $P = 1.4 \mu\text{m}$ ) array is shown.  $S$  is calculated via truncated numerical evaluation as described in section 2. The grating transition wavelengths are indicated by the dotted vertical lines. (b) Computed extinction efficiency for a single ellipsoidal particle (black curve) and a 2D array of  $10 \times 10$  particles (red curve) via the CD method are shown. (c) Shifting in resonant wavelengths with varying periodicity for the on-substrate and embedded arrays are shown. Analytically obtained grating transition wavelengths for Si-(1,0), Si-(1,1), Si-(2,0) are also shown with dashed lines. Dotted blue/red lines correspond to the individual nanorod antenna resonance of on-substrate/embedded arrays. (d) Embedded 800 nm long nano-rods with  $1.5 \mu\text{m}$  periodicity displays perfect transmission in the vicinity of a grating transition wavelength.

Figure 5(a,b) presents an analysis of these higher order resonances using CD method for a two-dimensional array consisting of nanorods completely surrounded with silicon medium ( $L = 800 \text{ nm}$ ). Appearance of the higher grating orders results in a sudden sign change and a sharp maximum in the imaginary and the real parts of the lattice sum  $S$ , respectively [Fig. 5(a)]. As shown in Fig. 5(b), dips in extinction efficiencies are observed at these grating transition wavelengths  $\lambda_{\text{Si}/\text{Air}}^{-(i,j)} = n_{\text{Si}/\text{Air}} p / \sqrt{i^2 + j^2}$ , where  $p$  is the array periodicity,  $n_{\text{Si}/\text{Air}}$  is the index of silicon/air, and  $(i,j)$  is the two-dimensional grating diffraction order. In Fig. 5(c), experimentally obtained resonance wavelengths are plotted for varying array periodicities for embedded (red points) and on-substrate (blue points) arrays. For embedded arrays, the spectral locations of the resonances are controlled by the array periodicity and closely follow the analytically derived grating transition wavelengths (dashed lines) corresponding to Si-(0,1), Si-(1,1) and Si-(0,2) grating orders. Slight deviation from the analytical model is likely due to the finite NA (0.4) of the IR-objective resulting in a beam spread.

On the other hand, resonance wavelengths of the on-substrate arrays do not show significant variation with changing periodicity (blue points) as a result of weaker diffractive coupling among particles. Instead, they slightly deviate from the random on-substrate array resonance (dotted blue line). Figure 5(d) shows extinction spectra obtained from periodic arrays consisting of 800 nm long rods embedded 200 nm beneath the silicon surface. A sharp

dip in extinction efficiencies, corresponding to a nearly perfect transmission, is clearly visible in the extinction spectrum for the embedded array with a periodicity of  $1.5 \mu\text{m}$  (red curve in Fig. 5(d)). This sharp dip, a sign for strong diffractive coupling as shown in Fig. 1(b), occurs when the real part of the lattice sum  $S$  is a maximum (as discussed in section 1). Such a feature is not observed in extinction spectra obtained from the nanorod arrays directly fabricated on the silicon substrates.

### 3.4 Enhanced near-field intensities with collective plasmonics

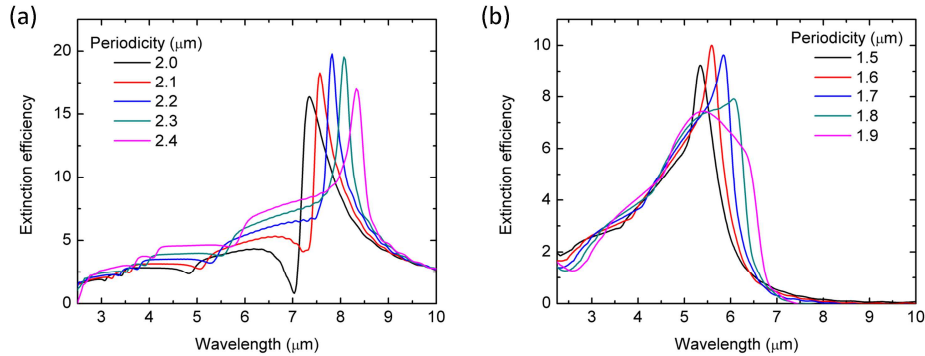


Fig. 6. 3D FDTD simulated extinction spectra are shown for (a) embedded ( $d = 200 \text{ nm}$ ) and (b) on-substrate nano-rod arrays for varying array periodicities ( $L = 800 \text{ nm}$  for both).

Far-field characteristics such as resonance linewidths and extinction efficiencies are a strong indicator of the near field behavior of the plasmonic excitations in relation to the plasmon lifetimes. Due to the suppression of the radiation damping with the confinement of the electromagnetic field within the array (extended plasmon lifetimes), narrowing of the far-field extinction resonances are observed. This narrowing is associated with the enhancement of the near-fields with respect to those of individual nanorods. In particular, when the array's diffractive resonances occur at a wavelength near the plasmon resonance of the individual particle, the collective plasmonic response is most pronounced. Near-field enhancements well beyond than those achievable with a single isolated particle are observed with optimized periodic arrays [5]. Considering that embedded nanoparticle arrays have even narrower resonances, much stronger near-field intensities are expected with respect to on-substrate fabricated arrays. This prediction is confirmed with 3-D FDTD simulations performed for the embedded structures consisting of  $800 \text{ nm}$  long rods buried  $200 \text{ nm}$  beneath the silicon surface as well as arrays of same size nanorods fabricated on-silicon substrate. The particles are modeled as  $100 \text{ nm}$  thick gold rods without the Ti adhesion layer used in the experiments. The calculated extinction efficiencies (shown in Fig. 6) illustrate the dramatic influence of the array periodicity on the resonance linewidths. The maximum amplitude of the extinction peak varies with the proximity of the array diffractive resonance to the particle LSPR [20]. The stronger extinctions for the embedded rods [Fig. 6 (a)] with respect that of the on-substrate ones are associated with the stronger diffractive couplings. The highest quality factors are observed at  $\lambda = 7.81 \mu\text{m}$  ( $5.68 \mu\text{m}$ ) for the embedded (on-substrate) arrays for the array with the periodicity of  $2.2 \mu\text{m}$  ( $1.6 \mu\text{m}$ ). The differences in resonance wavelengths of the embedded and on-substrate arrays are due to the differences in effective refractive indices. In agreement with our experimental observations (Fig. 4), narrowing of the resonance linewidths is much more pronounced in embedded arrays with respect to on-substrate ones.

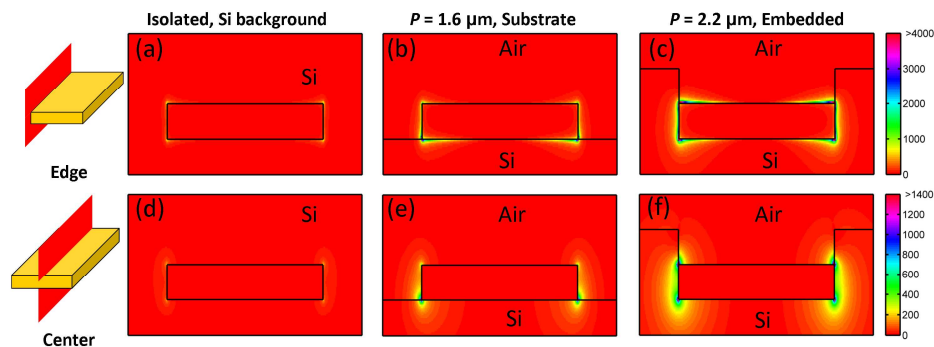


Fig. 7. Spatial distributions of the near-field intensity enhancements ( $|E/E_0|^2$  where  $E_0$  is the incident pulse amplitude at the corresponding frequency) for an isolated nanorod particle in homogenous silicon background (1st column), in a periodic array fabricated on silicon substrate (2nd column), and in a periodic array embedded in 200 nm beneath the silicon substrate (3rd column). Note the different color scales for edge (top row) and center vertical cuts (bottom row) planes indicated in red in the cartoons to the left.

The near-field intensities for individual nanorods in optimized arrays with the narrowest line-widths are shown in Fig. 7. Both embedded and on-substrate periodic arrays show marked improvements in near field enhancements with respect to the isolated nanorods. However, strongest overall near-field enhancements are observed for embedded structures as a result of longer plasmon lifetimes. For the arrays fabricated on silicon surface, the enhanced near-fields are mainly concentrated in a small region at the base of the nanorod. For the embedded geometry, a peak enhancement of 6,439 is obtained which extends over a large region outside the metal, while the enhancement of the on-substrate rod geometry is reduced to 3,579 outside the metal with lesser extent. The field distribution of the embedded structure is highly symmetric and closely resembles to that of the particle in homogeneous background. This implies the minimal effect of the air gap on the plasmon resonance. The large field enhancement extends over several tens of nanometers into the substrate as well as into the air gap.

For biodetection applications, the field enhancement in the air gap would be of primary interest. Despite the fact that the available region for target biomolecules is limited to the air gap region, the embedded geometry still offers advantages over on-substrate geometry. To quantify the effect, we have computed the integrated near-field intensity over the exposed surface of the embedded and on-substrate structures within a region extending 5 nm from the metal surface. The integrated intensity for the embedded geometry over this region is 2.2 times that of the on-substrate rods. Thus, despite the smaller exposed region, the embedded geometry should prove more advantageous due to the larger overall field enhancement. Finally, we note that the large enhancement in the dielectric medium (silicon substrate in this case) could also be extremely attractive for photovoltaic and nonlinear photonic applications.

#### 4. Conclusions

In summary, we experimentally demonstrated that plasmon lifetimes and extinction efficiencies can be controlled by tuning the retarded dipolar couplings among nanoantennas in periodic arrays. We observed embedded arrays lead to longer plasmon lifetimes and higher extinction efficiencies with respect to on-substrate fabricated ones. We have analyzed our experimental observations through analytical derivations and 3-D FDTD simulations. We show that these observations are indicative of stronger radiative couplings associated with the more homogeneous dielectric background present in the embedded particle arrays. Through numerical simulations, the correlation between the extended lifetimes of the plasmons and the enhancement of the near field intensities is confirmed. Near-field enhancements well beyond than those achievable with isolated nanoparticles are predicted. The introduced fabrication

method and proposed structure could be readily extendable to visible and near-infrared frequencies. Given the advantages of our approach and its inherent flexibility, these results should be of interest to the plasmonic applications utilizing large field enhancements as well as narrower resonances.

### **Acknowledgments**

This work is supported in part by NSF SGER Award (ECCS-0849603), Massachusetts Life Science Center New Investigator Award, NSF Engineering Research Center on Smart Lighting, Boston University Photonics Center and Army Research Laboratory.